Coherent vortices in rotating flows: A laboratory view

A. Longhetto[1], L. Montabone[1][2], A. Provenzale[2], H. Didelle[3]
C. Giraud[4], D. Bertoni[1] and R. Forza[1]

[1] *Dipartimento di Fisica Generale, Università degli Studi di Torino*
    V. P. Giuria 1, 10125, Torino, Italy
[2] *Istituto di Scienze dell'Atmosfera e del Clima, CNR - C.so Fiume 4, 10133, Torino, Italy*
[3] *Equipe "Coriolis", LEGI-IMG - 21 Av. des Martyres, 38041, Grenoble, France*
[4] *Istituto di Fisica dello Spazio Interplanetario, CNR - Corso Fiume 4, 10133 Torino, Italy*

"(...) ast illam ter fluctus ibidem torquet agens circum, et rapidus vorat aequore vortex."
"(...) thrice round the ship was toss'd, then bulg'd at once, and in the deep was lost."
P. Vergilius Maro, *Aeneis,* I, 116-117

Summary. — We discuss a series of laboratory experiments on the dynamics of long-lived coherent vortices in rapidly rotating flows. The experiments have been carried out on the "Coriolis" large-scale rotating platform (14 m of diameter) of the LEGI-IMG in Grenoble (France), with the aim of understanding a) how vortices evolve; and b) how to characterize the vortex ability to trap passive tracers for long times. In this work we describe the technical aspects of the different experiments and discuss some of the properties of vortex dynamics and of particle dispersion.

PACS 92.10.Lq – Turbulence and diffusion.
PACS 47.32.Cc – Vortex dynamics.
PACS 47.27.Jv – High-Reynolds-number turbulence.

1. – Introduction

Turbulent rotating flows are characterized by the presence of long-lived coherent vortices [1-6a]. In this context, "coherent" means that the vortex lifetime is much larger than a typical eddy turnover time. Geophysical examples of this type of structures include Gulf Stream Rings, the salty Mediterranean eddies called "Meddies", tropical cyclones, and the stratospheric polar vortex.

Coherent vortices form easily in rotating flows, due to several instability mechanisms. In particular, a random initial vorticity field can self-organize into a set of long-lived vortices that dominate the dynamics of the flow and emerge as individual entities from the turbulent background.

In past years, coherent vortices have been shown to be strongly impermeable to inward and outward particle fluxes, being able to trap passive tracers for long times and providing a possible mechanism of anomalous transport that is absent in unstructured turbulence [7, 8]. The cores of coherent vortices are also characterized by the absence of Lagrangian chaoticity [9]. Additionally, coherent vortices induce non-Gaussian velocity distributions in the surrounding turbulent field [6b], requiring significant modifications of stochastic models of particle dispersion [10]. Because of these characteristics, coherent vortices can play an important role in determining the properties of tracer transport in the ocean and the atmosphere.

For the above reasons, in the past ten years the dynamics of coherent vortices has been intensively studied, from both numerical and experimental points of view, see, *e.g.*, [3-5] for reviews. In the present work we describe a set of laboratory experiments designed to study the dynamics and transport properties of long-lived coherent vortices in a quasi–two-dimensional framework. These experiments represent a continuation of our previous experimental work on cyclogenesis and on the interaction of turbulent flows with obstacles, see Alessio *et al.* [11-13] and Longhetto *et al.* [14].

The experiments presented in this paper have been carried out on the "Coriolis" platform of the LEGI-IMG (Laboratoire des Ecoulements Géophysiques et Industriels) in Grenoble, France. This platform supports a large circular tank (diameter of 13 m) which allows for obtaining large coherent vortex structures and for reaching small values of the Rossby number. This paper is devoted to the description of the experimental set-up and of the different kinds of measurement techniques employed. We also present some clear and sharp images of vortices in rapidly-rotating flows and of the related particle dispersion processes. A quantitative analysis of the experimental results will be reported in a forthcoming paper.

In sect. **2** we describe the experimental set-up and the flow visualization techniques for mapping the instantaneous flow fields. Section **3** is devoted to the presentation and discussion of images from the experiments and of some of the results obtained by using the Particle Image Velocimetry (PIV) technique. Conclusions are drawn in sect. **4**.

2. – Experimental set-up

2˙1. *The "Coriolis" rotating hydraulic tank of the LEGI-IMG in Grenoble.* – The large rotating "Coriolis" platform of the LEGI-IMG supports a circular tank with a diameter of 13 meters and a depth of 1.2 meters. The tank rotation period can be adjusted continuously from about 20 to 1000 seconds. The tank can be filled, up to about 180 t, either with homogeneous fluid (fresh or salt water) or with stratified fluid, by using different concentrations of salt. The maximum total weight of the facility is of the order of 300 t. The platform is supported in its center by a spherical thrust bearing, and in its periphery by 23 rollers equally spaced around the circumference. The discrepancy from the vertical is about $3 \cdot 10^{-6}$ rad.

Water temperature and salinity of water are stabilized and controlled with high precision, due to the thermal inertia of such a large amount of fluid. Water is introduced from the bottom while the table is rotating. In stratified experiments fresh water is introduced first, followed by salt water. In order to avoid excessive mixing, the tank is filled in approximately 4-5 hours. Additional 2-3 hours are allowed for the fluid to spin up to approximate solid body rotation; residual motions in the tank, due to convection and wind stress effects, are estimated to be of the order of 0.5 cm·s^{-1}.

2˙2. *Description of the experiments*. – The present experiments are devised to explore the dynamics of an incompressible, homogeneous and rapidly-rotating shallow fluid. The fluid layer has a free surface and a flat bottom. Only an initial forcing is introduced, then the initial energy decays by dissipation. For rapid rotation, the flow tends to become two-dimensional and the horizontal velocity tends to become non-divergent.

Simple boundary conditions for the study domain are obtained by using a closed rectangular channel, 8.4 m long and 4 m wide, placed in an off-diameter position in the main circular tank. Figure 1a provides a top view of the tank, of the channel and of the study domain.

In order to generate the initial flow, two strategies are followed. In the first one, we generate a quasi-random initial condition by moving forward and backward a rigid frame of equally spaced, vertical flat teeth, that we call the "rake." Each tooth has a height of 1 m. The initial input of energy occurs at a length scale which depends on the spacing between the rake teeth and the individual tooth width. The horizontal spacing between two neighboring teeth is chosen to be either 17.5 or 35 cm and the tooth width is respectively 5 or 10 cm. Since the rake has a total length equal to the smaller side of the rectangular tank, a total of 18 or 9 vertical teeth are used. Figure 1b provides a view of the system. The initial quasi-random turbulent field is then generated by a computer-controlled movement of the rake along the tank, obtaining what we call "rake turbulence", *i.e.* a quasi–two-dimensional analog of "grid turbulence." Of course, the initial turbulence has a three-dimensional structure anyway, and it is only the rotation of the system that eventually generates an almost two-dimensional motion at later times (after a few minutes).

As a second generation method, specifically designed for this kind of experiment, we use a cylinder with diameter of 1 m, that is hanged from a small rotating hand-crane, allowing to lower it in the water at pre-determined positions in the tank. The cylinder is equipped with four rotating flat blades that allow for spinning up the water inside the cylinder, with a period corresponding to the desired turnover time of the vortex. In this way one can generate a vortex with specific characteristics at a pre-selected location and inject dye and individual tracers directly inside the vortex core. With this method, it is impossible to obtain a pure cyclonic or anticyclonic vortex, and for cyclonic rotation inside the cylinder a tripole is generally formed.

Different values for the control parameters of the flow are obtained by varying the speed of motion of the rake, the water depth and the rotation period. This leads to different values for the initial Rossby and Reynolds numbers and for the Rossby deformation radius, which are summarized in table I. Here, the Rossby number is defined as $Ro = U/fL$, the Reynolds number is $Re = UL/\nu$ and the Rossby deformation radius is $R = \sqrt{gH}/f$, where U is the velocity scale of the flow, L is the horizontal length scale, H is the fluid depth, $f = 2\Omega$ is the Coriolis parameter (Ω is the angular velocity of the tank), ν is the dynamic viscosity and g is the acceleration of gravity. In order to estimate the initial value of these numbers, we use the speed of the rake as the velocity scale and the mean between the spacing between two rake teeth and their width as the length scale. Later on, the dominant length scale becomes the vortex radius (that is larger than the rake spacing and the tooth width), the velocity becomes smaller due to dissipation, and the Rossby number decreases, down to an order of $O(10^{-1})$.

After generation, the turbulence has a freely-decaying evolution. Coherent structures emerge from the background and develop into long-lived vortices. The interactions among the vortices lead to merging or coupling events, and the size of vortices increases up to about 1 m in diameter. Each run is recorded for at least 40 minutes, corresponding to
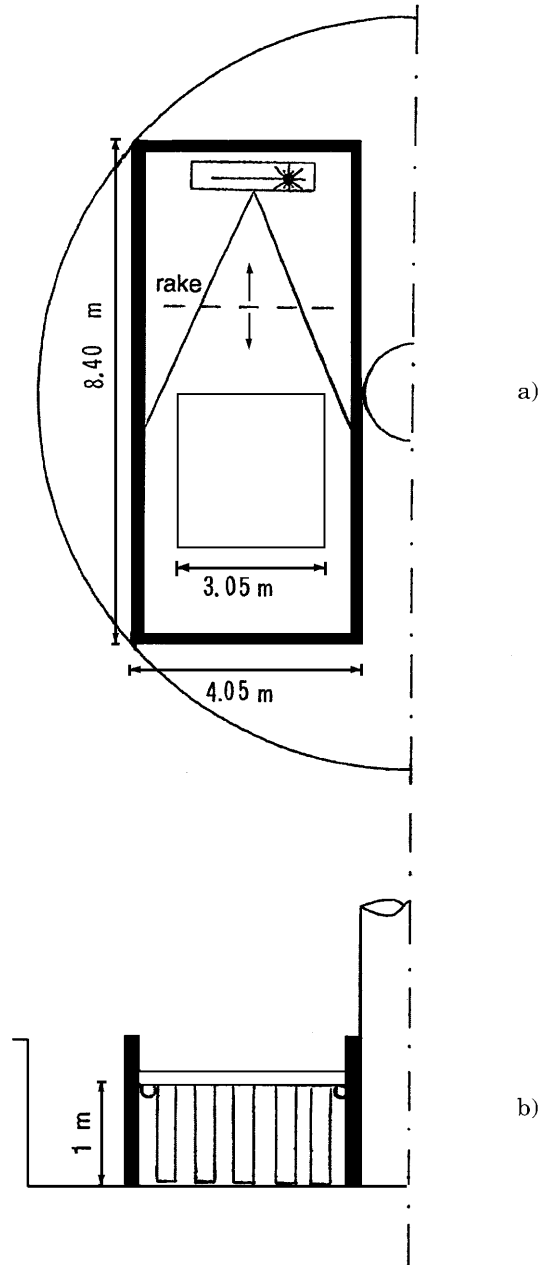
Fig. 1. – Top view (a) and cross-section (b) of the rotating tank with the experimental set-up. In the top view, the channel and the study domain are shown. In the cross-section, we show a schematic picture of the rake.

TABLE I. – *Values of the initial Rossby and Reynolds numbers and of the Rossby deformation radius. These are determined by the different values of the experimental parameters which are used, namely the tank rotation period, the water depth, the horizontal velocity of the vertical rake and the spacing between two teeth in the rake. The initial velocity and length scales are chosen as, respectively, the speed of motion of the rake and the mean between the teeth spacing and their width.*

Rotation period T(s)	Water depth H(m)	Rake speed U(cm/s)	Rake spacing (cm)	Initial Rossby number $Ro = U/fL$	Initial Reynolds number $(\times 10^4)$ $Re = UL/\nu$	Rossby deformation radius $R = \sqrt{gH}/f$ (m)
50	0.90	13	35	2.3	2.9	11.8
		6.5	35–17.5	1.1–2.3	1.5–0.7	
		3.25	35–17.5	0.6–1.1	0.7–0.4	
		1.62	35	0.3	0.4	
100	0.90	6.5	35–17.5	2.3–4.6	1.5–0.7	23.6
		3.25	35–17.5	1.1–2.3	0.7–0.4	
		1.62	35	0.6	0.4	
50	0.35	13	35–17.5	2.3–4.6	2.9–1.5	7.4
		6.5	35–17.5	1.1–2.3	1.5–0.7	
		3.25	35–17.5	0.6–1.1	0.7–0.4	
100	0.35	13	35	4.6	2.9	14.8
		6.5	35–17.5	2.3–4.6	1.5–0.7	

more than 50 rotations of the tank.

Particular care is devoted to test the hypothesis of a quasi–two-dimensional flow. A qualitative confirmation of the two-dimensionality of the flow is obtained during the experiments, as the laser beam positioned at different vertical levels in the fluid shows the same structure on the different horizontal planes. More quantitatively, the estimated values of the horizontal divergence are close to zero, as discussed further below. This happens for both the slower (period of 100 s) and the faster (period of 50 s) tank rotation speed and it becomes more clear as the turbulence evolves.

2˙3. *Observation and measurement techniques.* – In order to obtain qualitative and quantitative measurements of the Eulerian characteristics of the flow, two techniques have been adopted: the *Particle Image Velocimetry* (PIV) and the *Laser Induced Fluorescence* (LIF) techniques. In addition, direct Lagrangian information is also obtained by using up to 25 float-like tracers, usually in combination with the LIF technique.

Particle Image Velocimetry or Digital Particle Image Velocimetry is used to measure the instantaneous velocity field in a planar section of the flow. The technique consists in determining the local displacements of patches of small passive tracers over a sufficiently small time interval in such a way that the mean velocities measured provide a close estimate of the global instantaneous velocity field. See Raffel *et al.* [15] for a review of the PIV technique, and Jambunathan *et al.* [16], Westeerweel *et al.* [17], Scarano and Riethmuller [18, 19] for recent improvements on the processing algorithms.

For the use of the PIV, we adopted the following experimental configuration:

– a continuous 8 W Argon laser source with a wavelength of 488 nm (green light).
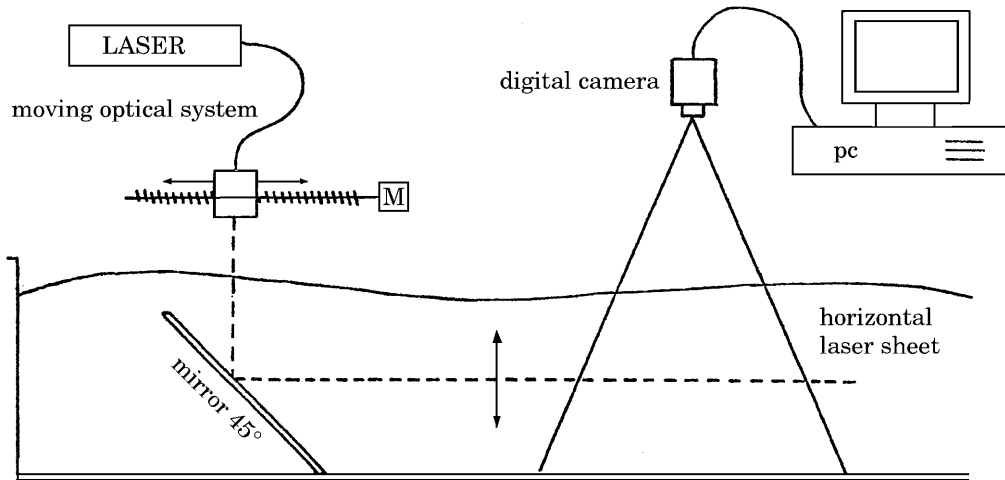
Fig. 2. – Experimental set-up for the use of PIV and LIF visualization techniques. A laser produces a coherent beam which is expanded in a sheet by using a deflecting mirror. Another mirror, set at 45° with respect to the ground, is used to expand the sheet horizontally. The horizontal laser sheet may be positioned at different vertical levels by acting on the moving optical system. A CCD camera captures images of a portion of the flow illuminated by the laser sheet, and the binary data are sent to a Personal Computer where they are stored.

    – A deflecting mirror (with an oscillation frequency of 120 Hz) in order to expand the laser beam into a laser sheet either in the horizontal or in the vertical plane. The sheet thickness is between 5 and 10 mm.

    – A dual channel cross-correlation Kodak Megaplus camera (model ES 1.0) with a CCD sensor having a pixel array of 1008(H)×1018(V) and a minimum pulse separation of 5 μs.

    – A personal computer equipped with a frame grabber and a very fast hard disk in order to collect and store the images at the maximum available frame rate (30 Hz).

The experimental set-up of this apparatus is shown in fig. 2, and the position of the (3.05×3.05) m^2 view field is shown in fig. 1a.

The flow is seeded uniformly with a mixture of 60 μ Orgasol and 150 μ Optimage particles (with a nominal density of about 1.02 g/cm^3). Special attention is paid to determine the numerical density of seeding particles (*seeding density*) in the channel, in order to obtain images with an optimum number of particles per pixel (p.p.p.). Fincham and Spedding [20] produce a plot of the optimum seeding density *vs.* particle diameter in the images for strong and weak shear. As the diameter of the image of the particles we use is $d \cong 3$ pixels and shear can be strong in the circulation cells around vortex cores, based on the above estimate we select a density of $N \cong 0.1$ p.p.p.

In the experiments described above, we use the cross-correlation technique to obtain particle displacements. To this end, on pre-selected times we record a "burst" of images, *i.e.* a series of frames containing the particle positions at different but closely-spaced times. The total recording time for each experiment is 40 minutes. During this period, a total of 80 bursts are recorded, at intervals of 30 seconds. Each burst is composed by

4 image frames taken with different time delays, aimed at having several possible combinations of particle displacements. This is designed to allow for choosing the best pair of frames during the following processing analysis. At the beginning of the evolution, when the velocities are high, we prefer to use frames that have a small time separation, while on later times we prefer to use frames with a larger time separation. In addition, time delays are linearly increased during the recording time, to approximately compensate for the turbulence decay and the consequent velocity decrease.

The *Correlation Image Velocimetry* (CIV) algorithm by Fincham and others is then used to obtain the Eulerian velocity on a grid by processing the raw PIV images. This algorithm incorporates advanced features that improve the performance and allow for obtaining accurate values for the velocities: the decoupling of the interrogation window from its fixed location in the first image to any arbitrary location in the cross-correlated second image, inside a search box; the possibility of performing a hierarchical scheme of multi-passes with increasing spatial resolution; the on-line correlation peak averaging of Hart [21] for reducing the wrong vectors. See Fincham *et al.* [22], Fincham and Spedding [20] and Fincham and Delerce [23] for details. Derived quantities, such as vorticity or horizontal divergence, can then be calculated from the velocity field using local splines.

An important point is the possible residual presence of wrong vectors (also called *outliers*) in the velocity field at the end of each correlation process, also after use of Hart's detection and correction in the first pass. These outliers have to be detected and filtered by the use of automatic numerical processes before each subsequent pass and before calculating the derivatives. We address the problem of outlier detection and filtering by developing an algorithm, additional to the main CIV algorithm, that improves their detection. The most used algorithms for the detection of an outlier need to evaluate the mean (or median) of its neighbours, together with the standard deviation, and use the latter as a threshold value for the difference between the interrogated vector and the mean (or median). However, the standard deviation itself can be affected by errors due to the possible presence of outliers in the nearby vectors. An appropriate "window function" is used to filter and correct the local standard deviation in order to fix the proper threshold value (see [24] for details). Filtered vectors are then interpolated by local splines.

Laser Induced Fluorescence (LIF) is the technique that we used to visualize the instantaneous flow structures and to tell apart the vortex cores from the turbulent background. The arrangement for using the LIF is the same used for PIV; the difference is the seeding, which is *Disodium fluorescein* (green dye) with an absorption wavelength of 500 nm and an emission wavelength of 535 nm. See Walker [25] and Aanen *et al.* [26] for details on this technique.

In order to get direct Lagrangian information, we also use a few float-like tracers composed by a buoyant stick and an approximately ellipsoidal container in the lower part (the balloon), see fig. 3. Iron pellets are placed inside the balloon, in order to equilibrate the float at a certain depth. We used floats with balloons at 20 cm depth. The particular shape of these floats avoids "sticking effects" due to surface tension. The floats are furnished with a fluorescent upper bright stick to visualize their path and to record their positions by the camera. The frame rate acquisition is in this case higher than for PIV. We record one frame every 5 seconds, for a total acquisition time of 14 minutes. A float tracking algorithm is used to identify the float positions and to obtain information on the dispersion properties of the turbulent flow. This algorithm is based on the searches for local maximum gray levels and particular care has been adopted in order to recognize
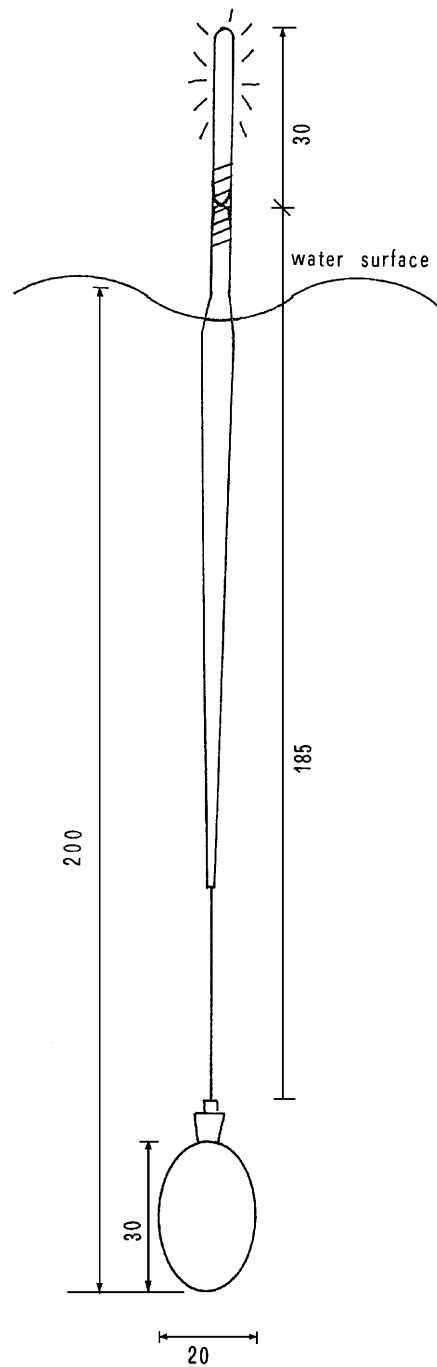
Fig. 3. – Sketch of a float-like tracer used as a Lagrangian tracer. It is composed by a buoyant stick and an ellipsoidal container in the lower part (the balloon). Iron pellets are placed inside the balloon, in order to equilibrate the float at a certain depth (20 cm). The floats have a fluorescent upper bright stick that is used to visualize the paths and to record the float positions by the camera. In the figure, units are in millimeters.
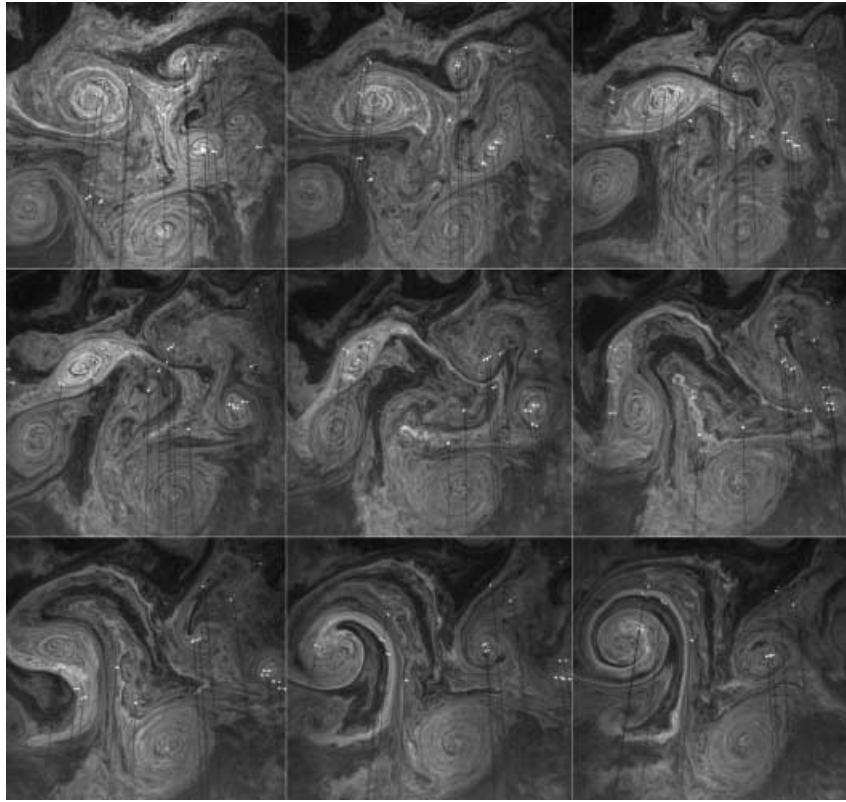
Fig. 4. – Sequence of flow visualizations obtained by LIF. Each snapshot represents the structure of the turbulent flow in a 3×3 m^2 area placed at a few centimeter below the free surface. The time interval between the snapshots is 50 s and the first snapshot is taken 6 min after the passage of the rake. In this experiment, the water depth is 90 cm and the rotation period is 50 s. The white dots are float-like tracers, whose shadows are visible as black straight lines.

floats that are very close to each other.

2˙4. *Data collection*. – During the experiments we collect three types of raw data:

– Photographic images and sequences of digital images of the fluid seeded with fluorescein. The flow structures are visible without any post-processing. It is possible to visually follow the time evolution of the coherent vortices and the displacement of the float-like tracers.

– Sequences of digital PIV images of the fluid seeded with microscopic particles. These images need post-processing in order to extract quantitative data on Eulerian velocity, vorticity, kinetic energy, horizontal divergence and other dynamical variables.

– Sequences of digital images of the position of the float-like tracers. Post-processing is necessary to get quantitative information on the float positions, for example to compute float dispersion.

The sequences of velocity fields obtained with PIV processing form a large data set available for detailed studies of the Eulerian properties of the vortices, as well as for studies of passive tracer transport. By interpolating in space and time these fields it is possible to numerically integrate the trajectories of individual Lagrangian particles.

3. – Vortex visualization and particle transport processes

In this section we present some examples of visualization of large-scale coherent vortices in quasi-2D flows, which could hardly be obtained on small rotating tables. Some results on the dispersion of passive tracers are also discussed.

Figure 4 shows how the use of LIF can reveal the structure of the turbulent field and pinpoint the presence of large-scale vortices. In this figure, each panel represents a snapshot of the flow structure in a horizontal 3×3 m^2 area placed a few centimeters below the free surface. These images refer to an experimental configuration with water depth of 90 cm, rotation period of 50 s, and rake with coarsely spaced teeth moving at 6.5 cm/s. This gives an initial Rossby number of about 1.1 and a Reynolds number of about 15000. The time interval between two consecutive snapshots is 50 s, and the first snapshot is taken 6 min after the passage of the rake.

The figure illustrates the vortex evolution. The forward and backward motion of the rake creates irregular lines of small-scale wake vortices, whose size depends on the teeth spacing and width. The initial three-dimensional turbulent component is rapidly damped out, due to the rotation of the tank, and after some minutes (between about 5 and 10, depending on the rotation period), the flow shows an overall "Taylor columns" structure. Vortices reinforce and aggregate with each other, increasing in size, whereas in the background the energy is rapidly dissipated. The main mechanism of aggregation is vortex merging, that is well represented in the sequence of fig. 4: when two barotropic vortices with the same sign approach each other at sufficiently small distance, a process of merging usually occurs [27]. In fig. 4, two merging processes are visible. The vortices are first deformed and vorticity filaments are emitted, then a rapid rotation around each other occurs and finally the two cores merge together, resulting in a single, almost axisymmetric vortex. The merging process appears to be quite fast in comparison with the advection of vortices by the turbulent field. The vortex in the lower part of the images, which is not involved in any merging process, does not move much during the whole sequence.

The use of LIF can, in our experiments, allow for a qualitative description of the dynamics of vortices and the dispersion of tracers (as discussed further below), but for a quantitative description the use of PIV is necessary. In fig. 5 we show, at two different (late) times, typical velocity and vorticity fields obtained from PIV measurements, for the same experiment shown in fig. 4. Both the decrease of the number of vortices and the growth of the vortex size are evident.

The use of PIV furnishes the global velocity field on a grid, that, in the case considered here, has a resolution of 64×64 grid points. It is thus possible to use these data for obtaining an estimate of the time evolution of the total energy, enstrophy and mean square divergence.

Thus, we observe that strong tracer trapping takes place in non-merging vortex cores, and this is associated with a well-defined impermeability of the vortex edge to inward and outward tracer fluxes.

The time evolution of the total energy and enstrophy, shown in figs. 6 and 7, indicates a decay that at late times can be approximated by a power law, $t^{-\alpha}$, with $\alpha = 1$ and
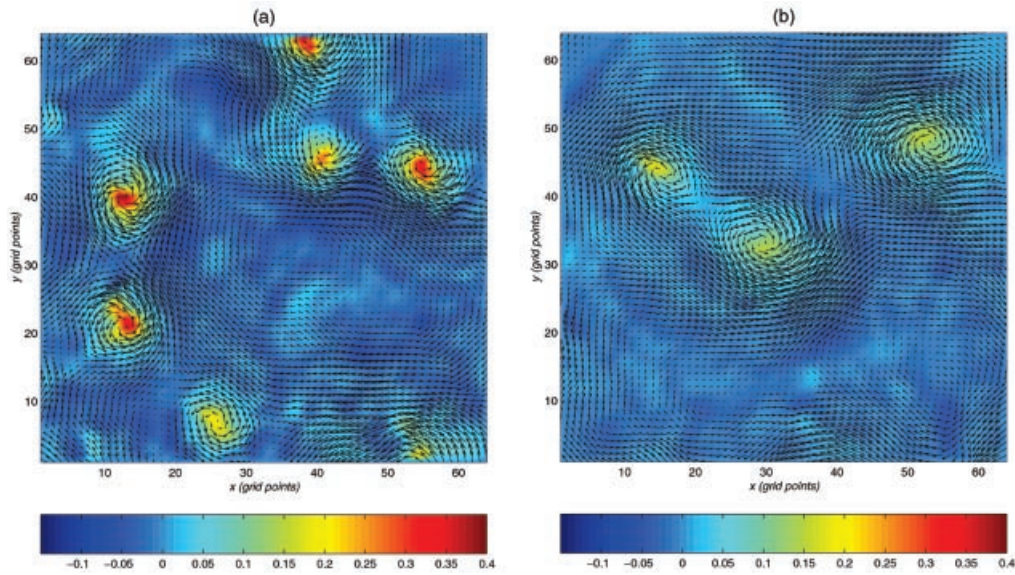
Fig. 5. – Velocity and vorticity fields obtained by PIV, for the same experiment of fig. 4. Panel (a) is at time $t = 11.5$ minutes after the arrest of the rake and panel (b) is at time $t = 30.5$ minutes. Arrows indicate velocities, while the color scale indicates vorticity ($\zeta = \partial v/\partial x - \partial u/\partial y$) in s^{-1}. The maximum modulus of velocity is 2.14 cm/s in panel (a) and 1.27 cm/s in panel (b). The velocity fields have 64×64 vectors, obtained by using an interrogation window of 32×32 pixels with 25% overlapping in each direction and by interpolating on a 64×64 grid. The spatial resolution in these figures is 4.5 cm.
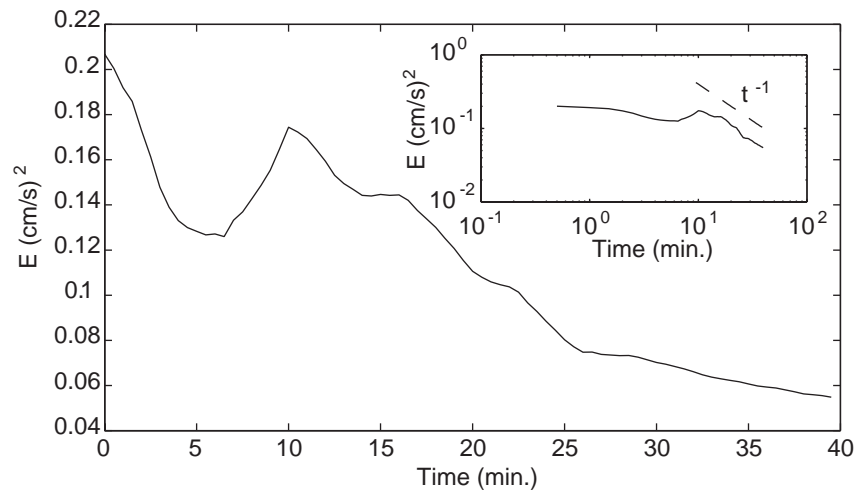

Fig. 6. – Time evolution of the total kinetic energy for the same experiment shown in fig. 5. The total kinetic energy is defined as $E = (1/A) \iint_A (1/2) \left(u^2 + v^2\right) \mathrm{d}x\mathrm{d}y$, where A is the domain area and (u,v) are the velocity components. In the inset, the scale is logarithmic and the dashed line is proportional to t^{-1}. The curve is smoothed by using a moving window average, with three values to the left and right of each value.
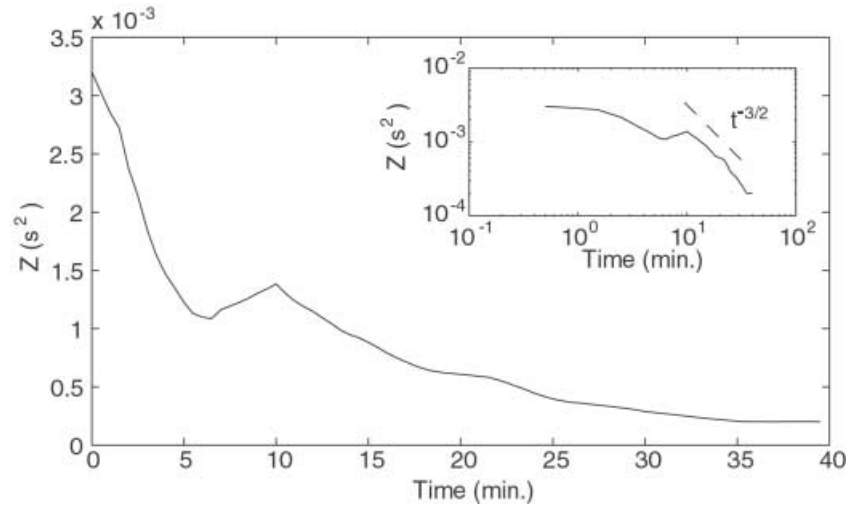
Fig. 7. – Time evolution of the total enstrophy for the same experiment shown in fig. 5. The total enstrophy is defined as $Z = (1/A) \iint_A \zeta^2 \mathrm{d}x\mathrm{d}y$, where A is the domain area and ζ is the vertical component of the vorticity ($\zeta = \partial v/\partial x - \partial u/\partial y$). In the inset, the scale is logarithmic and the dashed line is proportional to $t^{-3/2}$. The curve is smoothed as in fig. 6.

$\alpha = 3/2$, respectively. At early times, the sudden growth in energy and enstrophy, visible in the figures, is due to the entry of new vortices in the field of view. This is due to the fact that the domain measured by the camera is open, and the total amount of energy and enstrophy can fluctuate. The time evolution of the mean square horizontal divergence, shown in fig. 8, confirms that, a few minutes after the arrest of the rake,
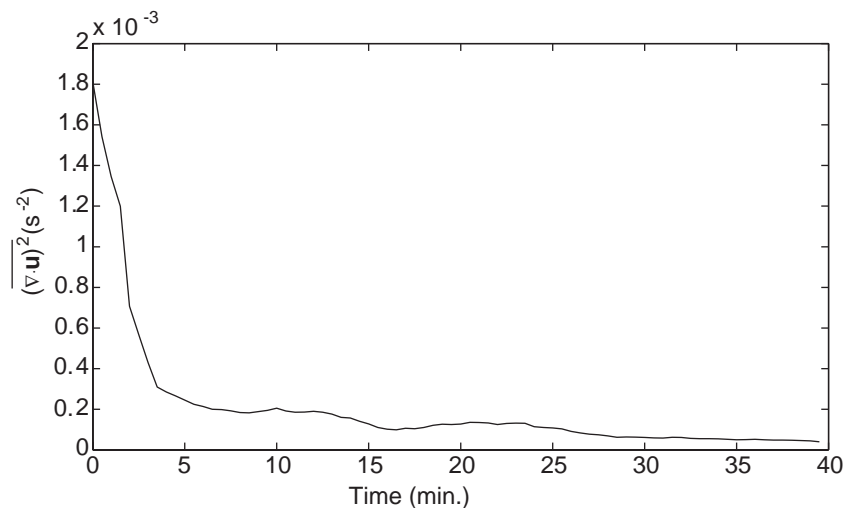

Fig. 8. – Time evolution of the mean square horizontal divergence, $\overline{(\partial u/\partial x + \partial v/\partial y)^2}$, for the same experiment shown in fig. 5. The curve is smoothed in the same way as in fig. 6, 7.
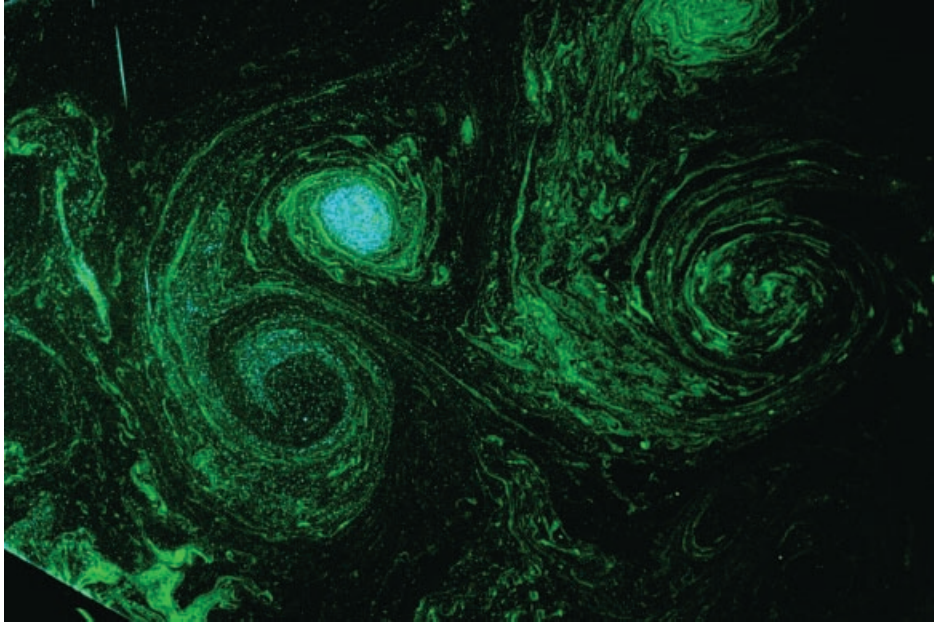
Fig. 9. – A picture of a dipole, where the core of the anticyclone has been seeded with PIV particles and the cyclone is unseeded. Fluorescein is seeded between the vortices. The core of the cyclone remains devoid of fluorescein.
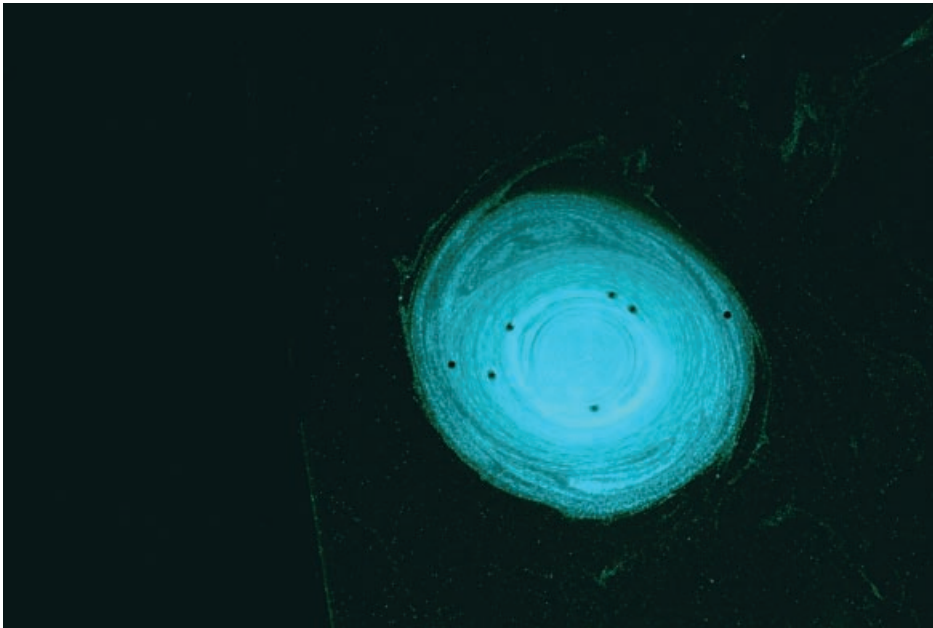

Fig. 10. – A picture of a monopolar vortex that has been created by using the cylinder with rotating blades. The tracers inside the vortex core (particles and float-like tracers) display a regular motion around the center.
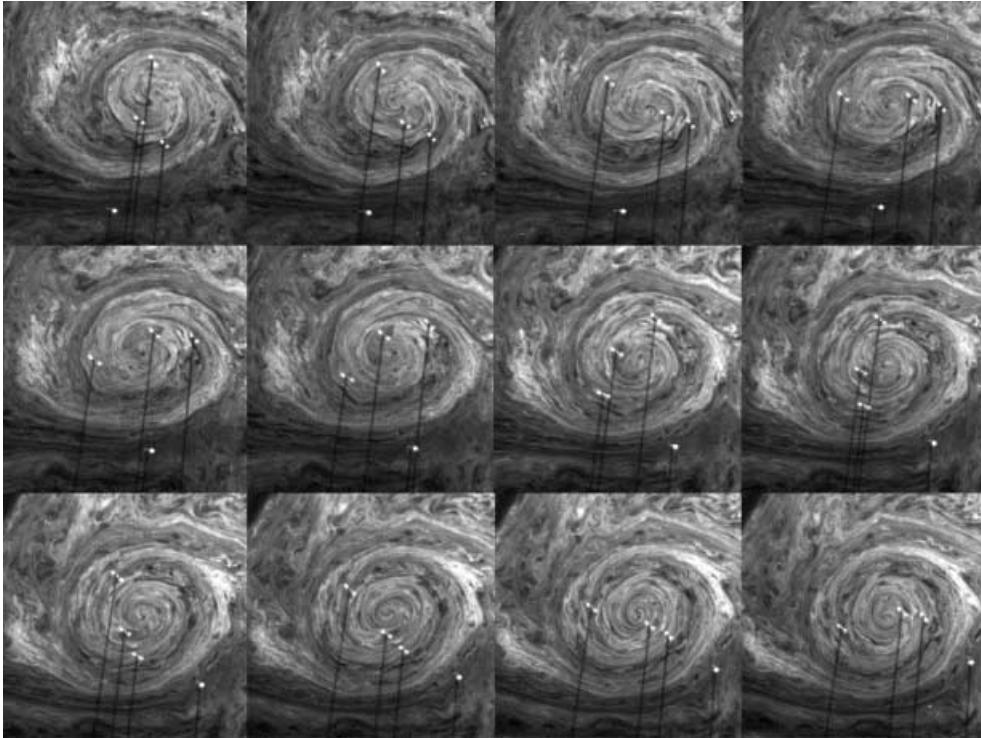
Fig. 11. – Evolution of an isolated cyclonic vortex, obtained by LIF. The snapshots are zooms of the vortex in the left upper part of the snapshots in fig. 4, before the merging process occurs. The time interval between the snapshots is 5 s and the first snapshot is taken 4 min after the passage of the rake. The white double dots are float-like tracers, whose shadows are visible as black straight lines. Double dots are a spurious effect due to the presence of the fluorescent sticks on the tracers.

the fluid becomes nearly two-dimensional, as the horizontal divergence becomes much smaller than the average r.m.s. vorticity.

Overall, the present experiments confirm that in rapidly rotating flows, quasi-random initial conditions evolve into vortices that are characterized by a long life-time. However, a strong asymmetry between cyclones and anticyclones is detected, contrary to what normally happens in pure barotropic turbulence at low Rossby number. In our experiments, cyclones are in general much stronger than anticyclones, and they live for a longer time. In a similar experimental set-up, Chabert D'Hieres *et al.* [28] observe that cyclones tend to show sharp circular boundaries, whereas anticyclones have no well-defined horizontal spatial structure. In their study, these authors also show that cyclonic vortices are reinforced, and anticyclonic vortices are destroyed for Rossby numbers of order one. Similar results are found in boundary layer experiments, see Tritton and Davies [29]. Lesieur [30] discusses the instability mechanism of a quasi–two-dimensional vorticity filament subject to a straining field, showing how cyclonic vortices survive while anticyclones are easily destroyed. A similar mechanism can be active in our experiment.

A further important point concerns the properties of particle transport. Figures 9 and 10 show vortices seeded with either fluorescein or with the microscopic particles
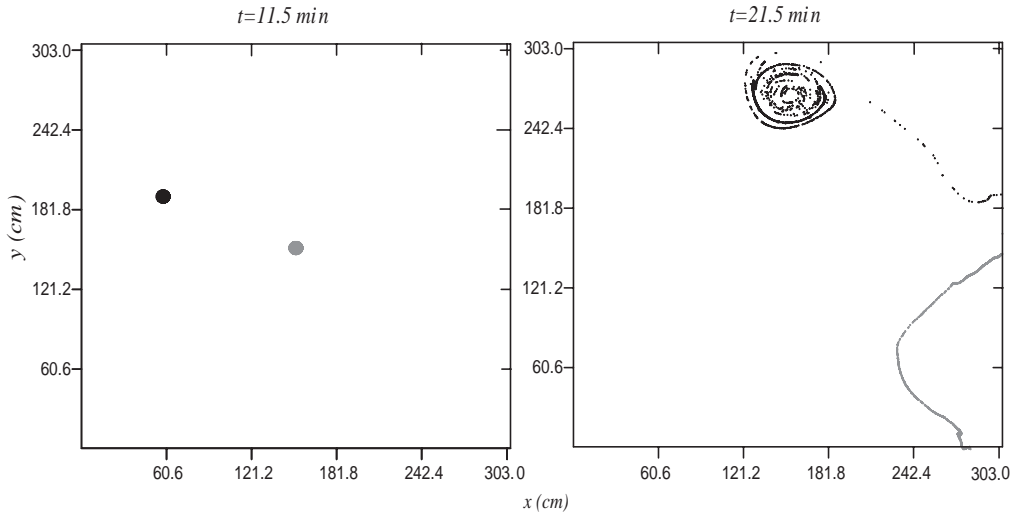
Fig. 12. – Snapshots of the positions of 1800 "numerical" Lagrangian particles seeded inside a cyclonic vortex (black dots) and 1800 particles seeded in the turbulent background (gray dots) at time $t = 11.5$ min after the arrest of the rake and at time $t = 21.5$ min, in the same experimental configuration as in fig. 5. The trajectories of the particles are numerically integrated by using the PIV Eulerian velocity fields interpolated in time and space. In the snapshot at time $t = 21.5$ min, particles (originally seeded in the background) that have reached the edge of the velocity field are not plotted.

used for the PIV. Figure 9 shows a situation where the core of the anticyclone in the dipole is seeded with PIV particles and the cyclone is unseeded. Fluorescein is seeded in the background. The core of the cyclone remains devoid of fluorescein. This latter does not enter the vortex except for molecular diffusion at late times. In fig. 10 we show the case of a vortex that is created artificially, by using the cylinder with rotating blades. The tracers inside the vortex show a regular rotational motion around the center, that is completely different from the chaotic particle advection present in the turbulent background between coherent structures [9, 5]. The fact that tracers seeded inside coherent vortices are trapped for long times is also evident in fig. 4, where the float-like tracers are represented by white points. This is further confirmed by the sequence of images shown in fig. 11. This sequence (corresponding to 55 s, approximately an eddy turnover time for this experiment) shows that the tracers inside vortices undergo only azimuthal relative dispersion and negligible radial dispersion.

The results of the observations are also confirmed numerically by using the PIV Eulerian velocity fields (interpolated in time and space) to integrate the trajectories of individual Lagrangian particles, according to the equation $\mathrm{d}\mathbf{X}/\mathrm{d}t = \mathbf{u}$, where $\mathbf{X} = (X, Y)$ is the position of a particle and $\mathbf{u} = (u, v)$ is the Eulerian velocity in this position. As an example, in fig. 12 we show the evolution of two patches of 1800 Lagrangian particles seeded at time $t = 11.5$ min respectively inside a cyclonic vortex (black dots) and in the background (gray dots) for the same experimental configuration shown in fig. 5. After 10 minutes, the particles seeded in the vortex have undergone azimuthal dispersion and slight radial dispersion but are still inside the coherent structure, whereas the patch seeded in the background has been elongated and stretched.

4. – Conclusions

Turbulence in rapidly rotating flows is characterized by the spontaneous emergence of long-lived coherent vortices. In past years, this problem has been extensively explored by the use of numerical simulations. In particular, simulations have shown that the vortex cores are characterized by strong impermeability to inward and outward particle fluxes, and are able to trap tracers for long times (see [5] for a review).

In this work, we have discussed the set-up of a series of laboratory experiments devoted to the study of the dynamics and transport behavior of quasi–two-dimensional coherent vortices. The experiments were performed in the large "Coriolis" rotating tank of the Laboratoire des Ecoulements Géophysiques et Industriels (LEGI-IMG) in Grenoble, France. In the course of the experiments, we obtained a large, high-quality data set on the dynamics of coherent vortices in a rapidly rotating barotropic fluid, which has been made possible by the use of a large-scale facility and the use of laser techniques for the flow visualization.

$$* * *$$

REFERENCES

[1] McWilliams J. C., *J. Fluid Mech.*, **146** (1984) 21.
[2] McWilliams J. C., *J. Fluid Mech.*, **219** (1990) 361.
[3] Hopfinger E. J. and van Heijst G. J. F., *Annu. Rev. Fluid Mech.*, **25** (1993) 241.
[4] McWilliams J. C. and Weiss J. B., *Chaos*, **4** (1994) 305.
[5] Provenzale A., *Annu. Rev. Fluid Mech.*, **31** (1999) 55.
[6] a) Bracco A., McWilliams J. C., Murante G., Provenzale A. and Weiss J. B., *Phis. Fluids*, **12** (2000) 2931; b) Bracco A., LaCasce J., Pasquero C. and Provenzale A., *Phys. Fluids*, **12** (2000) 2478.
[7] Rhines P. B. and Young W. R., *J. Fluid Mech.*, **133** (1983) 133.
[8] Elhmaidi D., Provenzale A. and Babiano A., *J. Fluid. Mech.*, **257** (1993) 533.
[9] Babiano A., Boffetta G., Provenzale A. and Vulpiani A., *Phys. Fluids*, **6** (1994) 2465.
[10] Pasquero C., Provenzale A. and Babiano A., *J. Fluid. Mech.*, **439** (2001) 279.
[11] a) Alessio S., Briatore L., Ferrero E., Giraud C., Longhetto A. and Morra O., *Boundary-Layer Meteorol. (Elsevier)*, **60** (1992) 235; b) *Nuovo Cimento C*, **15** (1992) 461.
[12] Alessio S., Briatore L., Ferrero E., Longhetto A., Giraud C. and Morra O., *Atmos. Environ. A*, **27** (1993) 2075.
[13] Alessio S., Briatore L., Cremonini R., Ferrero E., Giraud C., Longhetto A., Morra O. and Purini R., *Nuovo Cimento C*, **18** (1995) 603.
[14] Longhetto A., Briatore L., Chabert D'Hieres G., Didelle H., Ferrero E. and Giraud C., *Exp. Fluids*, **22** (1997) 387.
[15] Raffel M., Willert C. E. and Kompenhans J., *Particle Image Velocimetry, a Practical Guide* (Springer-Verlag, Berlin Heidelberg) 1998.
[16] Jambunathan K., Ju X. Y., Dobbins B. N. and Ashfort-Frost S., *Meas. Sci. Technol.*, **6** (1997) 507.
[17] Westerweel J., Dabiri D. and Gharib M., *Exp. Fluids*, **10** (1997) 181.
[18] Scarano F. and Riethmuller M. L., *Perfectionnement dans les techniques de traitement des données en vélocimétrie par images de particules*, in *Actes 6$^{\text{ème}}$ Congrès Francophone de Vélocimétrie Laser (1998), Saint-Louis (France)*.

[19] SCARANO F. and RIETHMULLER M. L., *Exp. Fluids*, **26** (1999) 513; *Advances in iterative multigrid PIV image processing*, in *3-rd International Workshop on Particle Image Velocimetry, September 16-18 (1999), Santa Barbara (USA)*.

[20] FINCHAM A. M. and SPEDDING G. R., *Exp. Fluids*, **23** (1997) 449.

[21] HART D. P., *The elimination of correlation errors in PIV processing*, in *9-th International Symposium on Application of Laser Techniques to Fluid Mechanics, July 13-16 1998, Lisbon (Portugal)*.

[22] FINCHAM A. M., SPEDDING G. R. and BLACKWELDER R. F., *Bull. Am. Phys. Soc.*, **36** (1991) 2692.

[23] FINCHAM A. M. and DELERCE G., *Exp. Fluids*, **29** (2000) S013.

[24] MONTABONE L., *Advanced outliers detection and filtering in particle image velocimetry*, in *Proceedings of the 3rd Pacific Symposium on Flow Visualization and Image Processing, March 18-21 2001, Maui, Hawaii (USA)*.

[25] WALKER D. A., *J. Phys. E*, **20** (1987) 217.

[26] AANEN L., TELESCA A. and WESTERWEEL J., *Machine Graphics & Vision*, **8** (1999) 529.

[27] MELANDER M. V., ZABUSKY N. J. and MCWILLIAMS J. C., *J. Fluid Mech.*, **195** (1988) 303.

[28] CHABERT D'HIERES G., DAVIES P. A. and DIDELLE H., *Laboratory studies of pseudo-periodic forcing due to vortex shedding from an isolated solid obstacle in a homogeneous rotating fluid*, in *Mesoscale/Synoptic Coherent Structures in Geophysical Turbulence* (Elsevier Science Publishers B. V., Amsterdam, The Netherlands) 1989.

[29] TRITTON D. J. and DAVIES P. A., *Instabilities in geophysical fluid dynamics*, in *Hydrodynamics Instabilities and the Transition to Turbulence*, edited by SWINNEY H. L. and GOLLUB J. P. (Springer-Verlag, Heidelberg) 1985, pp. 181-228.

[30] LESIEUR M., *Turbulence in Fluids* (Kluwer, Dordrecht) 1993.